A computationally efficient statistically downscaled 100 m resolution Greenland product from the regional climate model MAR

Marco Tedesco[1,2], Paolo Colosio[3], Xavier Fettweis[4] and Guido Cervone[5]

[1]Lamont-Doherty Earth Observatory, Columbia University, New York, 10964, USA

[2]NASA GISS, New York, 10025, USA

[3]Department of Civil, Environmental, Architectural Engineering and Mathematics, University of Brescia, Brescia, 25123, Italy

[4]Department of Geography, SPHERES research unit, University of Liège, Liège, 4000, Belgium

[5]Institute for Computational and Data Sciences and Earth and Environmental Systems Institute, The Pennsylvania State University, University Park, PA, 16801, USA

Correspondence to: Marco Tedesco (mtedesco@ldeo.columbia.edu)

Abstract. The Greenland Ice Sheet (GrIS) has been contributing directly to sea level rise and this contribution is projected to accelerate over the next decades. A crucial tool for studying the evolution of surface mass loss (e.g., surface mass balance, SMB) consists of regional climate models (RCMs) which can provide current estimates and future projections of sea level rise associated with such losses. However, one of the main limitations of RCMs is the relatively coarse horizontal spatial resolution at which outputs are currently generated. Here, we report results concerning the statistical downscaling of the SMB modeled by the Modèle Atmosphérique Régional (MAR) RCM from the original spatial resolution of 6 km to 100 m building on the relationship between elevation and mass losses in Greenland. To this goal, we developed a geospatial framework that allows the parallelization of the downscaling process, a crucial aspect to increase the computational efficiency of the algorithm. The results obtained in the case of the SMB, surface and air temperature are assessed through the comparison of the modeled outputs with in-situ and satellite measurements, show a considerable improvement in the case of the downscaled product with respect to the original, coarse output with the coefficient of determination (R^2) increasing from 0.868 for the original MAR output to 0.935 for the SMB downscaled product. Moreover, the value of the slope and intercept of the linear regression fitting modeled and measured SMB values shifts from 0.865 for the original MAR to 1.015 for the downscaled product in the case of the slope and from the value -235mm w.e. yr-1 (original) to -57 mm w.e. yr-1 (downscaled) in the case of the intercept, considerably improving upon results previously published in the literature.

1 Introduction

The Greenland Ice Sheet (GrIS) has been contributing directly to sea level rise since the beginning of the century through meltwater runoff and ice mass loss. Hörhold et al. (2022) found that modern temperatures over North and Central Greenland are 1.5 °C warmer than the twentieth century and that meltwater run-off, a major contributor to sea level rise, has been consequently enhanced. The duration of surface melting as well as melt extent have also been increasing since 1979, as measured by passive microwave satellite observations (e.g., Tedesco et al. 2013, Colosio et al., 2021). Moreover, Hanna et al. (2021) found that over the 1972-2018 period each 1°C of summer warming corresponds to 116 Gt of surface mass loss and 26 Gt of solid ice discharge increase. A key tool for studying the evolution of surface mass loss (e.g., surface mass balance, SMB) over the GrIS is represented by (polar) regional climate models (RCMs), which, differently from remote sensing observations (that can provide information about surface height changes but are unable to attribute height change to a mass change without more information about snow/firn compaction, e.g., Smith et al., 2023) can provide information on the mass loss and represent an irreplaceable tool to provide future projections of such losses. A widely used model in this regard is the Modèle Atmosphérique Régional (MAR, Fettweis et al., 2013, 2017, 2020; Tedesco et al., 2013)., a coupled surface-atmospheric model forced at its boundaries with reanalysis data. However, one of the limitations of MAR (and of RCMs in general) lies in the horizontal spatial resolution at which outputs can be generated. This is due to computational considerations as well as to the physics behind the models. Currently, MAR simulations over Greenland are generated at a horizontal spatial resolution of 6 km (e.g., Colosio et al., 2021). Such spatial resolution does not allow capturing fine-scale processes occurring in areas characterized by complex topography (e.g., glaciers terminating in fjords) or small glaciated surface (e.g., ice caps). Moreover, the knowledge of mass loss at a horizontal spatial resolution higher than the one currently available (e.g., 100s of meters) might allow a better characterization of the spatial inputs of runoff and freshwater to the surrounding oceans.

To address the limitations associated with the current horizontal spatial resolution of the MAR model, statistical downscaling can be used to enhance the spatial resolution of the modeled outputs. For example, Hanna et al. (2005, 2008, 2011) statistically downscaled reanalysis data over the GrIS. A statistical downscaling technique based on elevation correction was also applied by Franco et al. (2012) to the 25 km MAR outputs to reconstruct GrIS SMB at 15 km spatial resolution. Following that, Noël et al. (2016) applied an elevation dependent statistical downscaling technique to SMB components simulated by the Regional Atmospheric Climate Model (RACMO2) at 11 km resolution to reconstruct a daily dataset of SMB over the GrIS over a 1 km resolution grid. Here, we build upon the approach proposed by Noël et al. (2016) to generate a 100 m, statistically downscaled output of MAR SMB over the whole GrIS. Beside applying the approach to a different set of modeled outs (MAR instead of RACMO) and the enhanced spatial resolution with respect to Noël et al. (2016), we developed a geospatial framework that allows the parallelization of the downscaling process which increases the computational efficiency of the algorithm. In the following, we first describe the datasets used for our approach (Section 2), then we introduce the methodology (Section 3), followed by the results (Section 4) and our conclusions and future work (Section 5).

2 Datasets

2.1 MAR Model

Modeled quantities to be downscaled are obtained from the regional climate model MAR (Colosio et al., 2021; Alexander et al., 2014; Fettweis et al., 2013; Fettweis et al., 2017; Tedesco et al., 2013). MAR is a modular atmospheric model that uses the sigma-vertical coordinate to simulate airflow over complex terrain and the Soil Ice Snow Vegetation Atmosphere Transfer scheme (SISVAT) (e.g., De Ridder and Gallée, 1998) as the surface model. The snow model in MAR, which is based on the CROCUS model of Brun et al. (1992), calculates albedo for snow and ice as a function of snow grain properties, which in turn depend on energy and mass fluxes within the snowpack. Lateral and lower boundary conditions are prescribed from reanalysis datasets. Sea-surface temperature and sea-ice cover are prescribed over the ocean using the same reanalysis data. The atmospheric model within MAR interacts dynamically with SISVAT. MAR outputs have been assessed over the GrIS by many authors (e.g., Fettweis et al., 2017, 2020; Alexander et al., 2014).

In this study, we use the output from MAR version v3.11.5 characterized by an enhanced computational efficiency and improved snow model parameters (Fettweis et al., 2020; Delhasse et al., 2020). The model is 6-hourly forced at the boundaries from 1950 using ERA5 reanalysis (Hersbach et al., 2020), the newest generation of global atmospheric reanalysis data that superseded ERA- Interim (Dee et al., 2011), and output is produced at a horizontal spatial resolution of 6 km. Specifically, we focus our attention on daily air temperature (TT variable, being the temperature above 2 m from the surface), surface temperature (ST variable) and surface mass balance (SMB) outputs.

2.2 Digital Elevation Model

For the Digital Elevation Model (DEM), we adopt the ArcticDEM data product (Porter et al., 2018, Figure 1). ArcticDEM is a National Geospatial-Intelligence Agency (NGA) and National Science Foundation (NSF) public-private initiative to produce high-quality DEM of the Arctic applying stereo auto-correlation techniques to high-resolution optical satellite images and adopting the SETSM open-source photogrammetric software (Noh and Howat, 2015). Further information about the dataset can be found at https://www.pgc.umn.edu/guides/arcticdem/introduction-to-arcticdem/. GrisSpecifically, we use a DEM provided at the spatial resolution of 100 m. The data are projected to the National Snow and Ice Data Center (NSIDC) Sea Ice Polar Stereographic North and referenced to WGS84 datum. The overall dataset is composed of 403,920,000 cells and is distributed as a GeoTIFF with a total size of approximately 1.6 Gb.

2.3 PROMICE Surface Mass Balance measurements

The main objective of this work is to obtain a high-resolution SMB dataset from the downscaling of the MAR model suitable for local (i.e., glacier scale) studies. Consequently, we carried out a validation of our results by comparing the original SMB outputs from MAR at a spatial resolution of 6 km and the downscale outputs at 100 m with in-situ SMB measurements.

89   For this purpose, we used the dataset collected by Machguth et al. (2016), containing 2955 SMB measurements from 46 sites,

90   reported in Figure 1 as blue dots and   available on GEUS Dataverse portal (Machguth, 2022; last access 16/02/2023). Such

91   a comprehensive   dataset spans from 1892 to 2015. From the 123 years, we focused our attention to the period 1980 - 2015

92   when the largest portion of the dataset is temporally located and the MAR outputs are available. From the 2955 measurements

93   we obtained 1982 suitable SMB measurements to be used for validation. The SMB measurements are carried out by computing

94   the difference of stake readings between two dates. The observations are identified by the measuring site (i.e., the area or

95   location, containing at least one measuring point), measuring point   (i.e., specific stakes, associated with multiple readings)

96   and the actual readings (i.e., the SMB measurement). In Table 1 we report the number of readings for each measuring site

97   considered, together with its coordinates (WGS 84) and time period when the measurements were collected. Measurement

98   periods are various, covering specific seasons (summer or winter SMB) or an entire year (annual SMB). In some cases, also

99   short-term (at least one month) and multi-year measurements are present. We reconstructed the SMB in correspondence of the

00   measurement location as an algebraic   sum of the daily simulated SMB between the start and end dates of the measurement.

01   In order, as a metric to assess the performance of the downscaled product, we compute the root mean squared error (RMSE)

02   and the least-square linear regression parameters (slope and intercept) between model outputs (SMB   original and

03   downscaled) and measurements.

04   **2.4 GC-Net air temperature**

05   To test the results of the applied downscaling procedure at local scale we also compare the values of near surface air

06   temperature obtained from MAR with in-situ measurements. We use data from the Greenland Climate Network (GC-Net;

07   Steffen et al., 1996), a set of Automatic Weather Stations (AWS) located all around the GrIS   and continuously measuring

08   air temperature, wind speed, wind direction, humidity, pressure, and other parameters. Since direct measurements of surface

09   temperature are not available as continuous records at multiple sites around Greenland, we use the air temperature records

10   measured at 3 m above ground level. Specifically, we consider 17 selected stations reported in Figure 1 as red triangles.

11   Specific location and elevation for each station are also reported in Table 2 in the Results section. The AWS thermometers

12   collect air temperature measurements at sub-daily temporal scale while MAR outputs are provided at daily temporal resolution.

13   Consequently, we compute daily average air temperatures for the comparison with the modeled   and downscaled near-

14   surface temperatures (TT variable).

15   **2.5 Landsat-8 surface temperature**

16   As in situ measurements are only available at point scale, it is not possible to assess the potential improvement of the

17   downscaling approach on spatially distributed fields. In the absence of spatially distributed, high spatial resolution SMB

18   outputs, we use surface temperature fields from seven different Landsat-8 scenes covering the Jakobshavn and the Helheim

19   Glaciers, acquired on 5 June 2015, 30 June 2015 (two images), 9 July 2015 (two images), 16 July 2015, and 18 July 2015. The

20 Landsat-8 surface temperature product has been available at 30 m spatial resolution since April 2013 and is generated from

21 Landsat Collection 2 Level-1 thermal infrared bands and other parameters obtained from satellite observations and reanalysis

22 data. The images were downloaded from the USGS Earth Explorer data portal (https://earthexplorer.usgs.gov/, last access

23 17/01/2023). We compared the Landsat-8 observations with the original and downscaled MAR outputs of surface temperature

24 (ST variable).

25 **3. Methods**

26 **3.1 Downscaling methodology**

27   We adopted the approach used by No.l et al. (2016), in which a statistical downscaling method was applied to

28 RACMO to achieve a 1-km horizontal resolution. Here, we use a similar methodology applied to MAR, but instead downscale

29 the product to 100 m horizontal resolution. The method exploits the potential dependency of the modeled variables (e.g.,

30 surface temperature, runoff) with elevation. In order, to overcome the large number of cells and reduce the computational time,

31 we parallelized the procedure through a combination of geospatial tools (in the software R) so that our approach can also be

32 used for near-real time generation of downscaled maps over a specific region of the GrIS .

33   The first step involves the calculation of the local dependency of the MAR outputs with respect to the elevation. For

34 this step we refer to the methodology proposed by Noël et al. (2016). Accordingly, we compute the local linear regression

35 (least squares) between the specific variable and the elevation (obtained from the MAR DEM) obtaining the values of slope

36 (m_{6km}) and intercept (q_{6km}). The linear regression is carried out for each pixel of the MAR 6 km resolution DEM using the

37 values of the adjacent pixels with a minimum of 6 points used for the regression. In the case of pixels with less than 5 adjacent

38 pixels (e.g., margins of the ice sheet), we compute m and q for that pixel by interpolation. Such regression is carried out for

39 every day and pixel of the region of interest. Figure 2 provides an example of such a procedure . Parallelizing such

40 procedure for each MAR pixel, we obtain the daily maps of m_{6km} and q_{6km} for the considered MAR output variable. Differently

41 from Noël et al. (2016), we downscale the SMB output of MAR directly, rather than downscaling the components of the SMB

42 (runoff and sublimation) and then approximating SMB as the sum of its components. We opted for this choice because we

43 found that downscaling directly SMB provides better performance of the downscaling when compared with in-situ

44 measurements. Then, the m_{6km} and q_{6km} maps are reprojected to the Polar Stereographic coordinate system which is used

45 by the DEM. The original MAR data are distributed by providing only the coordinates for the center of each grid cell. To

46 create a continuous grid, and avoid introducing errors, the coordinates for the four corners of each MAR grid are computed,

47 and then they are transformed into the Polar Stereographic coordinate system. The result is a shapefile that contains a polygon

48 for each MAR grid. Additionally, the new shapefile contains metadata to ease computations, such as a unique MAR grid ID,

49 the Polar Stereographic coordinates for the center of the grid, the corresponding coordinates in longitude and latitudes for

50 the center of the grid. The next step consists in fragmenting the high-resolution DEM into a series of smaller files,

51 specifically one for each polygon of the reprojected MAR cells generated in the previous steps. There are a total of 55,144

files generated through each step, which are less than the total number of cells in the original MAR output. This discrepancy is due to the fact that the DEM is limited to only areas covered by the ice sheet, and it thus does not cover all the locations of where MAR output is generated. While it might seem counterintuitive that maintaining over 55,000 small files is more efficient than maintaining a single file, the answer lies in the fact that this preprocessing step translates our problem into a parallelization one that can be efficiently solved using multi-core and multi-node infrastructure. Because the DEM is required for downscaling each grid cell, which are computed simultaneously in parallel, each task needs to read only a small file of a few kb, rather than one larger file, and it also avoids file system bottlenecks when multiple processes try accessing the same file. Most file systems do not allow for concurrent access to the same file, and therefore if hundreds of tasks try to read the same file, each task would have to idle in a queue for the file access to become available. This problem is prevented by generating a DEM file for each MAR grid, so that both input/output transfer rate and file access are optimized. Furthermore, because the DEM are segmented using the original Polar Stereographic projection, which matches the reprojected MAR grid, no further transformation is required, further speeding up the downscaling process. The final step consists in obtaining the high-resolution maps of slope and intercept (m_{100m} and q_{100m}) by bilinear interpolation of m_{6km} and q_{6km} over the high-resolution DEM grid. While this process was not parallelized in the current version, it is possible to speed it up using a parallel solution. Finally, the downscaled variable is obtained by applying the high-resolution linear regression coefficients to the high-resolution DEM as

$$VAR_{100m} = m_{100m}H_{100m} + q_{100m}, \tag{1}$$

where VAR is the generic downscaled variable computed as a linear function of high-resolution elevation of the DEM (H_{100m}) through the coefficients previously obtained (m_{100m} and q_{100m}). Since the origin of the MAR DEM and the high-resolution DEM is different, errors in terms of mass conservation can arise. For example, within a MAR pixel the average elevation of the high-resolution DEM might be higher than the original MAR elevation, possibly leading to the previously mentioned mass conservation error (e.g., the original MAR pixel suggests for a day a lower mass loss than the ensemble of the high-resolution pixels). For this reason, differently from Noël et al. (2016), we decided to provide physical constraints (SMB mass conservation within each pixel at the original MAR spatial resolution) to be satisfied as the very final step of the downscaling procedure.

In this research, we apply the downscaling methodology to daily near-surface temperature, surface temperature and SMB MAR outputs .

3.2 Spatial autocorrelation analysis and variograms

Beside RMSE, slope and intercept, we also focus on evaluating the potential improvements of the downscaled product with respect to the original coarser resolution MAR outputs in terms of capability to describe the spatial distribution of the considered variable. To this aim, we perform a spatial autocorrelation analysis using variograms. Variogram analysis is generally adopted in geostatistical analyses to evaluate autocorrelation of spatial data (Edward et al., 1989, Webster and Oliver, 2001). Autocorrelation and variogram analysis are geostatistical tools that can be used to quantify spatial variability using metrics such as the spatial correlation length (simply correlation length hereafter). Though these techniques were mainly designed to support the prediction of values at locations where measurements are not available, they can be used for characterizing processes across the scale spectrum (Herzfeld, 1993). Once process scales are known, the scale ranges over which process relationships (and thus spatial pattern) are consistent must be determined. This can support the identification of spatial scales at which the process interactions change (e.g., scale breaks), being such scales critical for measurement or model interests (Mark and Aronson, 1984; Vedyushkin, 1994). Geostatistical methods such as spatial covariance, variogram analysis, and spectral analysis (Webster and Oliver, 2001) quantify the spatial pattern of variability of an observed property over a scale range from the minimum sample separation to the distance at which the variable becomes spatially independent. This quantified variability can, then, be used for spatial estimation based on a finite number of data points. In our case, we fit the experimental variogram with a circular model, as this is the model that provided us with the highest R^2 when fitting the experimental data. The formal expression of the experimental variogram can be written as:

$$\gamma(\delta) = \frac{1}{2N(\delta)} \sum_{i,j \in N(\delta)} (x_i - x_j)^2, \qquad (2)$$

where γ is the semi-variance, $N(\delta)$ is the number of data pairs (*i-th* and *j-th*) distanced by d while x_i and x_j are the corresponding variable values. The fitting spherical function is, then, used to compute the three main parameters characterizing the variogram: the sill, the range and the nugget effect. The sill is defined as the maximum value at which the fitted curve becomes flat; such variance value is reached at a certain distance called *range,* beyond which the data are no longer autocorrelated. The range can be seen as a scale break (where data are no longer correlated). Of course, there can also be several scale breaks before the sill is reached, depending on the drivers controlling the modeled process. The nugget corresponds to $\gamma(0)$ and it should be ideally 0. The departure from 0 can be interpreted as the result of measurement errors or highly localized variability (Webster and Oliver, 2001). Following Colosio et al. (2021), we focus our attention on the range, the descriptor of the correlation length, comparing the range values computed for the original MAR temperature outputs, the downscaled temperature and the surface temperature observed by Landsat-8.

12   To further investigate and quantify possible improvements in terms of spatial description of the variable of interest by the

13   downscaled product, we also compute the so-called Structural Similarity Index Measure (SSIM). Such an index   has been

14   introduced by Wang et al. (2004) to provide a similarity measure between two images. This index can objectively quantify a

15   qualitative aspect such as the   similarity between two images. Considering a pair of images (X,Y) to be compared, the values

16   assumed by the SSIM are bounded by a unique maximum (SSIM(X,Y)=1) in case X=Y, otherwise SSIM(X,Y)<1. We compute

17   such a similarity   index for both original and downscaled MAR ST outputs, considering as reference the Landsat-8 surface

18   temperature image.

4 Results and discussion

4.1 Surface and near-surface temperature

21   We first tested the downscaling algorithm with the MAR near-surface temperature outputs. We compared the results

22   obtained with air temperature measurements from 17 AWS of the GC-Net. We performed the comparison by computing RMSE

23   and R^2 between the modeled   (original and downscaled) and the observed variable. The results obtained for the original

24   MAR and the downscaled temperatures are reported in Table 2. Both R^2 and RMSE obtained for the downscaled temperatures

25   do not exhibit significant improvements or worsening with respect to the original coarser resolution output. The difference

26   between the 6 km and 100 m resolution is in the order 10^{-3} for R^2 and 10^{-2} °C for RMSE, with improvements in some stations

27   (Swiss Camp, Crawford Pt. 1, NASA-U, Summit, Crawford Pt. 2, KAR, JAR2 and KULU) and worsening in others (Tunu-N,

28   JAR1, South Dome and NASA-E). However, such small differences appear to be randomly distributed in space, without any

29   clear correlation with elevation or latitude/longitude. Such results demonstrate that the applied downscaling methodology does

30   not introduce errors in case of the TT variable at point scale.

31   To evaluate the results over a wider area, we considered two Landsat-8 surface temperature images collected over

32   two different areas of the ice sheet. The two selected areas are located on the eastern and western coasts of Greenland and

33   show a variable topography. In Figure 3 we report the surface temperature image from Landsat-8 (Figure 3a), the original ST

34   output at 6 km spatial resolution (Figure 3b) and the downscaled ST at 100 m resolution (Figure 3c) for one of the selected

35   Landsat-8 scenes.   In Figure 4 where we report the histograms of the difference between Landsat-8 surface

36   temperature and the original ST (Figure 4a) and the downscaled one (Figure 4b) for the same image. The results show no

37   differences in terms of mean difference (μ), with an average difference of 2.7°C in both cases, similarly to the AWS

38   comparison. Also, the standard deviation (σ) remains unvaried   at   2.6 °C. Similar results have been obtained for all the

39   compared Landsat-8 images, with mean differences ranging between -0.59°C and 3.44°C for the downscaled product (2.09°C

40   on average) and between -0.62°C and 3.43°C for the original MAR data (2.07°C on average). The similarity in mean

41   differences is not surprising   considering the physical constraints   imposed for the ST to maintain the average ST constant

42   for each MAR pixel as the final   step of the downscaling procedure. These results indicate that in case of ST the downscaling

algorithm does not introduce significant improvements or errors in terms of overall difference with observed temperature (expressed as RMSE for the AWS case and spatial average difference for the Landsat-8 image).

Considering such results in terms of difference at point scale and spatially averaged difference, we evaluated possible improvements in terms of spatial information content and spatial description obtained in the downscaled product. We report in Figure 5 the results of the variogram analysis performed for two sub-regions of interest within the same Landsat-8 image shown in Figure 3. The two areas have been selected because of the strong differences in topography and elevation gradients. Concerning the results obtained over the topographically more complex area, we observe that the scale break of the downscaled temperature (blue line) is 13.5 km, better capturing the one from Landsat-8 data (11.5 km, red line) with respect to the original MAR outputs (24.1 km, black line, Figure 5). On the other hand, the same analysis performed over an area in a more interior region of the ice sheet, where downscaling might lead to less improvement in view of the reduced topography, does not present improvements in terms of spatial autocorrelation (Figure 5b) and that all three datasets do not reach the variogram plateau within the considered distance. In order to extend the comparison to another area of the ice sheet, we performed the same variogram based analysis for another Landsat-8 scene in the surroundings of Jakobshavn glacier collected on 11 June (Figure 6a). The map also shows the two regions of interests (ROI) selected for the analysis. We selected ROI_1 as this area is characterized by a large topographic gradient within a relatively small distance and to understand the potential improvement of the downscaling procedure over regions that are outside the main ice sheet (e.g., smaller glaciers). On the other hand, ROI_2 contains both strong and mild elevation gradients (e.g., nunataks and ice sheet elevation gently increasing as moving towards the interior). In case of ROI_1 (Figure 6b), the variogram analysis indicates that the scale break distance for Landsat-8 when considering only the pixels where the DEM is available is 7.5 km. This value becomes 14.6 km for the high-resolution map of ST and 24.7 km in the case of the original MAR outputs, suggesting that the downscaled product is able to perform better than the original one in terms of spatial scale similarity with respect to the Landsat-8 data. The mean difference between Landsat-8 and the downscaled (original MAR) surface temperature, considering only the pixels where the DEM is available, are 1.69 ºC (1.7 ºC) with a standard deviation of 2.02 ºC (2.14 ºC), with differences of the same order of magnitude obtained in the previous analysis for the other Landsat-8 image. When considering all pixels within the ROI (e.g., also where no DEM is available), the mean differences between Landsat-8 and downscaled (original) MAR surface temperature become 1.89 ºC (2.12 ºC) with a standard deviation of 2.15 ºC (2.23 ºC). In this case, the scale breaks for the original and the downscaled MAR versions are similar, ~ 25 km (~ 16km in the case of Landsat-8). We point out that the scale breaks are sensitive to the different physical processes driving the spatial properties. The ROI_2 contains both strong and mild elevation gradients given the presence of nunataks and the slow ice sheet increasing elevation after the ice cliff begins. The area is covered by most of its portion containing the ice sheet (right of the image) by the DEM, which, however, is absent in the case of the left portion of the ROI, containing fjords and the ocean. The scale breaks for the Landsat-8, downscaled and original MAR cases for the portion of the ROI_2 where the DEM is available are close to each other, on the order of ~ 25 km. We observe an improvement in the SSIM in the case of the downscaled data by 30 % (from 0.33 in the case of the original MAR resolution to 0.43 in the case of downscaled MAR). Unexpectedly, despite the mean and standard deviation of the distribution of the differences between

the Landsat-8 data and the simulated quantities remains similar, we notice a reduction in both the mean (from 0.86ºC for original MAR to 0.83ºC for the downscaled product) and of the standard deviation (from 0.71ºC for original MAR to 0.63ºC for the downscaled product) when downscaling the MAR output. We further note that when considering all pixels (including those where no DEM), the SSIM of the two products improves from 0.11 (original) and 0.14 (downscaled) and that the scale break of the original MAR products is larger (~ 63 km) than the one of the Landsat-8 data (~ 21 km). In synthesis, the downscaling does not introduce any considerable bias on the original value, preserves the total integrated quantity of energy within each area and improves the spatial performance of the MAR outputs by generating a product that has a spatial structure that is closer to the one of the observed remote sensing dataset.

4.2 Surface Mass Balance

After applying the downscaling algorithm to surface temperature, we applied it to MAR SMB outputs of SMB and assessed the results obtained with in situ measurements from the dataset collected by Machguth et al. (2016). As mentioned, we compared 1982 SMB measurements carried out between 1980 and 2015 and localized in the ablation area of the GrIS (Table 1). Figure 7 shows the scatterplots of the comparison of modeled SMB from the original MAR (Figure 7a) and the downscaled product (Figure 7b) with in situ measured SMB. Our results show that the downscaled product better estimates the measured SMB, exhibiting an increased R^2 from an already relatively high value of 0.868 for the original MAR to 0.935 for the downscaled product. As a comparison, Noël et al. (2016) obtained an increase of R^2 from the downscaling of SMB outputs of the RACMO regional climate model from 0.47 in the case of the original 11 km spatial resolution outputs to 0.78 in case of the downscaled SMB (1 km resolution). As explained in Fettweis et al. (2020), the SMB was extrapolated (interpolated + corrected) to the common 1km grid by applying an elevation gradient as done in this study. One of the key issues raised by the first SMB model intercomparison performed by Vernon et al. (2013) was the high dependency of modeled integrated SMB values to the ice sheet mask used. To mitigate this problem, we interpolate all model outputs to the same 1 km grid used in the Ice Sheet Model Intercomparison Project for CMIP6 (ISMIP6). This resolution is chosen because the highest resolution model outputs (e.g. RACMO2.3p2) are available at 1 km and choosing a coarser resolution could compromise their quality. A common grid also allows a comparison on two common ice sheet masks: the contiguous Greenland Ice Sheet, which is common to all the models and the Greenland Ice Sheet plus peripheral ice caps and mountain glaciers, common to all the models except the two PDD models. Unless otherwise indicated, the SMB components have been interpolated to 1 km using a simple linear interpolation metric of the four nearest inverse-distance-weighted model grid cells. Moreover, as done in Le clec'h et al. (2019), the interpolated 1 km SMB and runoff fields have been corrected for elevation differences between the model native topography and the GIMP 250 m topography (upscaled to 1 km here), using time- and space-varying SMB–elevation gradients, similar to Franco et al. (2012) and Noël et al. (2016). No correction was applied to precipitation after interpolation to 1 km. We point out that, in our case, the starting value of R^2 for the original MAR product already exceeds the value obtained in the case of the downscaled RACMO outputs.

09   The values of slope and intercept of the best-fitting line improve as well when considering the downscaled product.

10 The value of the slope shifts from 0.865 for the original MAR to 1.015 for the downscaled product; similarly, the intercept

11 increases from the value -235 mm w.e. yr-1   of the coarse resolution outputs to -57 mm w.e. yr-1   of the downscaled

12 SMB, closer to its optimal value (i.e., null intercept). As a comparison, the downscaling algorithm of Noël et al. (2016) applied

13 to RACMO improved the estimate of SMB in terms of slope   from 0.72 to 1.03, with a slight increase of the intercept (from

14 70 mm w.e. yr-1   to 100 mm w.e. yr-1   ). The RMSE between modeled   and measured SMB also decreases in the case

15 of the downscaled product from 669 mm w.e. yr-1   for the 6 km outputs to 511 mm w.e. yr-1   for the 100 m case,

16 significantly improving the estimate of SMB at local scale. Noël et al. (2016) obtained a reduction of the RMSE passing from

17 a value of 1200 mm w.e. yr-1   for the 11 km RACMO outputs to a value of 740 mm w.e. yr-1   for the 1 km case. Fettweis

18 et al. (2020) compared MAR and RACMO, among 13 models of four types (positive degree day models, energy balance

19 models, regional climate models and general circulation models), SMB estimates with the same PROMICE in situ

20 measurements within the GrIS SMB model intercomparison project (GrSMBMIP). They considered only the measurements

21 collected between 1980 and 2012 and with measurement periods   longer than 3 months. They also excluded the records

22 located outside the 1 km ice mask they used for the intercomparison of the models, for a total of 1438 SMB measurements.

23 The model versions in this case are MARv3.9.6, an older version than the one we adopted and at the spatial resolution of 15

24 km, and RACMO2.3p2 (Noël et al., 2019), a new version of the one adopted in Noël et al. (2016) and with a spatial resolution

25 of 5.5 km. From the comparison, they obtained a RMSE of 480 mm w.e. yr-1   for MAR and 630 mm w.e. yr-1   for

26 RACMO. In both cases, the RMSE is lower than the one obtained in this work for MAR (both original and downscaled) and

27 by Noël et al. (2016) for RACMO. The difference can be related to the differences in spatial resolution and model versions

28 and, most probably, to the sub-sampling of the SMB measurements discarding short-term records (i.e., measurement period

29 lower than 3 months), suggesting that the bias might be dissipated for longer observation periods.

30   To further investigate our results, we compute the variation in RMSE between the 6 km spatial resolution MAR

31 outputs and the downscaled product for different elevation classes, longitude and latitude ranges and for each specific

32 glacier/location (i.e., for each station ID, Table 1) of the PROMICE in situ SMB dataset. The RMSE difference is computed

33 as $\Delta RMSE = RMSE_{100\ km} - RMSE_{6km}$ (i.e., improvements are characterized by negative values of $\Delta RMSE$) and the results

34 obtained are reported in Figure 8 grouped by location (Figure 8a), elevation (Figure 8b), latitude (Figure 8c) and longitude

35 (Figure 8d). The results exhibit improvements in the estimate of SMB at all the altitudes besides the 100-200 m asl, 200-300

36 m asl and 1300-1400 m asl elevation classes, with the best performance obtained at 700-800 m asl and 800-900 m asl elevation

37 classes. The results grouped by latitudinal bands show the highest improvements in south Greenland; a decrease in performance

38 has been recorded in the latitudinal band 67.5-70 °N where the only Paakitsoq JAR ($\Delta RMSE=$ 181 mm w.e. yr-1   , worst

39 result obtained) and Swiss Camp/ST2 ($\Delta RMSE=$ -127 mm w.e. yr-1) measurement sites are located, and the improvement

40 obtained in case of Swiss Camp is strongly counterbalanced by the reduced performances in Paakitsoq JAR. However, the

41 longitudinal classes do not present any decrease of the performances, indicating that the worsening in the spotted critical

42 stations is counterbalanced by the improvements measured in the others. We obtained a decrease in performances in 6 out of

22 considered cases with the worst result obtained for the already presented Paakitsoq JAR case. In the 5 other cases (i.e., Hans Tausen Ice Cap, Nioghalfvjerdsfjorden, Isortoq , Nordbo Glacier and K-Transect) we recorded an average ΔRMSE of 26 mm w.e. yr-1 (ranging from 6 mm w.e. yr-1 to 80 mm w.e. yr-1). On the other hand, we obtained an improvement in 16 out of 22 measurement sites with the best performances in the case of A.P. Olsen Ice Cap (ΔRMSE= -611 mm w.e. yr-1). In the other 15 cases (i.e., Qaanaaq Ice Cap, Petermann, Hare Glacier, Kronprins Christian Land, Storstrømmen, Freya Glacier, Violin Glacier, Helheim, Isortuarssup Sermia, Qamanarssup Sermia, Kangilinnguata Sermia, Qapiarfiup, Amitsuloq Ice Cap, Tasersiaq and Swiss Camp/ST2) we found an average decrease in RMSE of 183 mm w.e. yr-1 (ranging between 59 mm w.e. yr-1 and 371 mm w.e. yr-1). Even if such reduction of performances in terms of SMB estimate accounts for 27% of the considered stations, it does not compromise the overall improvement, being smaller in terms of average, minimum and maximum absolute values of ΔRMSE than the results obtained for the stations where improvement occurred.

5 Conclusions and future work

We applied a statistical downscaling technique to increase the horizontal spatial resolution of the outputs of the MAR regional climate model from 6 km to 100 m for the surface temperature and SMB quantities. The approach builds on the dependency of such quantities on elevation, as originally proposed in Noël et al. (2016). Here, however, the technique was applied to the output of a different climate model (RACMO) and the spatial resolution of the downscaled product was 1 km, rather than 100 m. Moreover, differently from Noël et al. (2016), we imposed a mass conservation so that the overall mass obtained for each pixel at high resolution nested within a coarse resolution one is preserved. To address the computational issues associated with the relatively high spatial resolution, we developed a geospatial, parallelized framework that allows us to perform the downscaling over the whole ice sheet in an efficient way.

We, first, tested our approach by applying it to surface temperature data and assessing the outputs using both in-situ and satellite data. Our results showed no significant improvement or deterioration of the downscaled product with respect to the original MAR outputs. This confirms that our approach was not introducing any bias and was properly implemented. However, we found improvement of the downscaled surface temperature when analyzing the skills of the downscaled product to capture the spatial scales (e.g., scale breaks) of the observed surface temperature fields. The results obtained in the case of the SMB show a considerable improvement in the case of the downscaled product with respect to the original, coarse output. In the case of the downscaled MAR product, the R^2 value increases from 0.868 for the original MAR to 0.935 for the SMB product with the value of the slope and intercept shifting from 0.865 for the original MAR to 1.015 for the downscaled product in the case of the intercept and from the value -235mm w.e. yr-1 of the coarse resolution outputs to -57 mm w.e. yr-1 in the case of the slope. As a reference, Noël et al. (2016) obtained an increase of R^2 from the downscaling of SMB outputs of the RACMO regional climate model from 0.47 in the case the original 11 km spatial resolution outputs to 0.78 in case of the downscaled SMB (1 km resolution) and a shift in the slope and intercept

75 from 0.72 to 1.03 (slope) and from 70 mm w.e. yr-1   to 100 mm w.e. yr-1   (intercept). An analysis of the performance of

76 the downscaled product for different elevation classes, longitude   and latitude ranges and for each specific glacier/location

77 where SMB in-situ data is available shows that the downscaled product does not perform as expected for 27% of the stations.

78 . However, we point out that   the deterioration of the performance over those stations (expressed in terms of changes

79 on the average error ΔRMSE) is much smaller than the improvement obtained in the remaining cases.

80 The next step is to implement a similar approach for downscaling MAR outputs over both the Greenland and

81 Antarctica ice sheet using machine learning (ML) based approaches. Indeed, the approach proposed here   cannot be easily

82 extended to Antarctica, where surface melting does not exhibit a strong dependency from elevation, as most of it occurs over

83 ice shelves, at the sea level and where little elevation gradients exist. Moreover, improvements to the downscaling of the SMB

84 can be obtained by either considering complementary inputs that can improve estimates of losses (e.g., remotely sensed albedo)

85 or of mass gains (e.g., accumulation). ML tools can help in this regard. ML tools have, indeed, been used for improving

86 predictions beyond that of state-of-the-art physical models or for improving parameterization in models. In particular,

87 conditional generative adversarial networks (C-GANs or simply GANs in the following) can be successfully applied to the

88 problems discussed above (Goodfellow et al., 2014). GANs is a class of ML tools in which two neural networks compete with

89 each other in a min-max optimization problem. The first network, called generator, aims to generate new data samples that are

90 indistinguishable from the training data (e.g., high-resolution melting maps obtained from the remote sensing observations)

91 by the other network, called discriminator. In our case the GAN aims to generate high-resolution melting maps that are

92 indistinguishable by the second network from high-resolution remote sensing observations or numerical model outputs. We

93 have already started to build the architecture for this framework and are in the phase of collecting the necessary datasets and

94 are building the proper data framework to perform such work.

95 **Code and data availability**

96 The MAR v3.11.5 code and outputs are available at https://www.mar.cnrs.fr/ and ftp://climato.be/fettweis/MARv3.11.

97 Automatic weather   station data are available on EnviDat portal (https://www.envidat.ch/#/metadata/gcnet, Steffen et al.,

98 2020, last access 16/02/2023). Surface mass balance measurements are available on GEUS Dataverse portal

99 (https://doi.org/10.22008/FK2/5VNBQA, Machguth, 2015, last access 16/02/2023). Landsat-8 images are available on the

00 USGS Earth Explorer portal (https://earthexplorer.usgs.gov/, last access 16/02/2023). Downscaled data is available at

01 https://doi.org/10.5281/zenodo.7803611. Downscaling code is available upon request to mtedesco@ldeo.columbia.edu.

Authors contributions

MT, PC and GC designed the study and the methodology. GC optimized the algorithm parallelization. PC and MT performed the comparison with measured and remotely sensed observations and wrote the first draft of the paper. XF ran the MARv3.11.5 model and provided the outputs. All the authors discussed the results and contributed to the paper.

Competing interests

Xavier Fettweis is a member of the editorial board of The Cryosphere,

Acknowledgment

This work was supported by the NASA grant 80NSSC17K0351, NSF grants OPP-1713072 and OPP-2136938 and the Heising-Simons Foundation grant HSFOUND 2019-1160. PC would like to thank Lamont-Doherty Earth Observatory and University of Brescia for the support provided.

References

Alexander, P. M., M. Tedesco, X. Fettweis, R. Van De Wal, C.J.P.P. Smeets, and M.R. Van Den Broeke: Assessing spatio-temporal variability and trends in modelled and measured Greenland Ice Sheet albedo (2000–2013). The Cryosphere, 8, 2293–2312, doi: 10.5194/tc-8-293-2014, 2014.

Brun, E., David, P., Sudul, M., and Brunot, G.: A numerical model to simulate snow-cover stratigraphy for operational avalanche forecasting, J. Glaciol., 38, 13–22, 1992.

Collection 2 Landsat 8-9 OLI (Operational Land Imager) and TIRS (Thermal Infrared Sensor) Level-2 Science Product Digital Object Identifier (DOI) number: /10.5066/P9OGBGM6. [Last access, 16/02/2023].

Colosio, P., Tedesco, M., Ranzi, R., and Fettweis, X.: Surface melting over the Greenland ice sheet derived from enhanced resolution passive microwave brightness temperatures (1979–2019), The Cryosphere, 15, 2623–2646, https://doi.org/10.5194/tc-15-2623-2021, 2021.

De Ridder, K. and Gallée, H.: Land Surface-Induced Regional Climate Change in Southern Israel, J. Appl. Meteorol., 37, 1470–1485, 1998.

Dee, D. P., Uppala, S. M., Simmons, A. J., Berrisford, P., Poli, P., Kobayashi, S., Andrae, U., Balmaseda, M. A., Balsamo, G., Bauer, P., Bechtold, P., Beljaars, A. C. M., van de Berg, L., Bidlot, J., Bormann, N., Delsol, C., Dragani, R., Fuentes, M., Geer, A. J., Haimberger, L., Healy, S. B., Hersbach, H., Hólm, E. V., Isaksen, L., Kållberg, P., Köhler, M., Matricardi, M., McNally, A. P., Monge-Sanz, B. M., Morcrette, J.-J., Park, B.-K., Peubey, C., de Rosnay, P., Tavolato, C., Thépaut, J.-N. and

Vitart, F.: The ERA-Interim reanalysis: configuration and performance of the data assimilation system, Q.J.R. Meteorol. Soc., 137(656), 553–597, doi:10.1002/qj.828, 2011.

Delhasse, A., Kittel, C., Amory, C., Hofer, S., van As, D., S. Fausto, R., and Fettweis, X.: Brief communication: Evaluation of the near-surface climate in ERA5 over the Greenland Ice Sheet, The Cryosphere, 14, 957–965, https://doi.org/10.5194/tc-14-957-2020, 2020.

Fettweis, X., Gallée, H., Lefebre, F. and van Ypersele, J.-P.: Greenland surface mass balance simulated by a regional climate model and comparison with satellite-derived data in 1990–1991, Climate Dynamics, 24(6), 623–640, doi:10.1007/s00382-005-0010-y, 2007.

Fettweis, X., Franco, B., Tedesco, M., van Angelen, J. H., Lenaerts, J. T. M., van den Broeke, M. R., and Gallée, H.: Estimating the Greenland ice sheet surface mass balance contribution to future sea level rise using the regional atmospheric climate model MAR, The Cryosphere, 7, 469–489, https://doi.org/10.5194/tc-7-469-2013, 2013.

Fettweis, X., Box, J. E., Agosta, C., Amory, C., Kittel, C., Lang, C., van As, D., Machguth, H. and Gallée, H.: Reconstructions of the 1900–2015 Greenland ice sheet surface mass balance using the regional climate MAR model, The Cryosphere, 11(2), 1015–1033, doi:10.5194/tc-11-1015-2017, 2017.

Fettweis, X., Hofer, S., Krebs-Kanzow, U., Amory, C., Aoki, T., Berends, C. J., Born, A., Box, J. E., Delhasse, A., Fujita, K., Gierz, P., Goelzer, H., Hanna, E., Hashimoto, A., Huybrechts, P., Kapsch, M.-L., King, M. D., Kittel, C., Lang, C., Langen, P. L., Lenaerts, J. T. M., Liston, G. E., Lohmann, G., Mernild, S. H., Mikolajewicz, U., Modali, K., Mottram, R. H., Niwano, M., Noël, B., Ryan, J. C., Smith, A., Streffing, J., Tedesco, M., van de Berg, W. J., van den Broeke, M., van de Wal, R. S. W., van Kampenhout, L., Wilton, D., Wouters, B., Ziemen, F., and Zolles, T.: GrSMBMIP: intercomparison of the modelled 1980–2012 surface mass balance over the Greenland Ice Sheet, The Cryosphere, 14, 3935–3958, https://doi.org/10.5194/tc-14-3935-2020, 2020.

Franco, B., Fettweis, X., Lang, C., and Erpicum, M.: Impact of spatial resolution on the modelling of the Greenland ice sheet surface mass balance between 1990–2010, using the regional climate model MAR, The Cryosphere, 6(3), 695-711, 2012.

Goodfellow, Ian J., Pouget-Abadie J., Mirza M., Xu B., Warde-Farley D., Ozair S., Courville A., and Bengio Y.: Generative adversarial networks, Commun. Acm, 63(11), 139-144, 2004.

Hanna, E., Huybrechts, P., Janssens, I., Cappelen, J., Steffen, K., and Stephens, A.: Runoff and mass balance of the Greenland ice sheet: 1958–2003, Journal of Geophysical Research: Atmospheres, 110(D13), 2005.

Hanna, E., Huybrechts, P., Steffen, K., Cappelen, J., Huff, R., Shuman, C., Irvine-Fynn, T., Wise, S., and Griffiths, M.: Increased runoff from melt from the Greenland Ice Sheet: a response to global warming, Journal of Climate, 21(2), 331-341, 2008.

Hanna, E., Huybrechts, P., Cappelen, J., Steffen, K., Bales, R. C., Burgess, E., McConnell, J. R., Steffensen, J. P., Van den Broeke, M., Wake, L., Bigg, B., Griffiths, M., and Savas, D.: Greenland Ice Sheet surface mass balance 1870 to 2010 based on Twentieth Century Reanalysis, and links with global climate forcing, Journal of Geophysical Research: Atmospheres, 116(D24), 2011.

Hanna, E., Cappelen, J., Fettweis, X., Mernild, S. H., Mote, T. L., Mottram, R., Steffen, K., Ballinger, T.J., and Hall, R. J.: Greenland surface air temperature changes from 1981 to 2019 and implications for ice-sheet melt and mass-balance change, International Journal of Climatology, 41, E1336-E1352, 2021.

Hersbach, H., Bell, B., Berrisford, P., Hirahara, S., Horányi, A., Muñoz-Sabater, J., Nicolas, J., Peubey, C., Radu, R., Schepers, D., Simmons, A., Soci, C., Abdalla, S., Abellan, X., Balsamo, G., Bechtold, P., Biavati, G., Bidlot, J., Bonavita, M., Chiara, G., Dahlgren, P., Dee, D., Diamantakis, M., Dragani, R., Flemming, J., Forbes, R., Fuentes, M., Geer, A., Haimberger, L., Healy, S., Hogan, R. J., Hólm, E., Janisková, M., Keeley, S., Laloyaux, P., Lopez, P., Lupu, C., Radnoti, G., Rosnay, P., Rozum, I., Vamborg, F., Villaume, S. and Thépaut, J. N.: The ERA5 global reanalysis, Quarterly Journal of the Royal Meteorological Society, doi:10.1002/qj.3803, 2020.

Hörhold, M., Münch, T., Weißbach, S., Kipfstuhl, S., Freitag, J., Sasgen, I., Lohmann, G., Vinther, B., and Laepple, T.: Modern temperatures in central–north Greenland warmest in past millennium, Nature 613, 503–507, 2023.

Le Clec'H, S., Quiquet,A. Charbit,S', Dumas, C., Kageyama, M. et al.. A rapidly converging initialisation method to simulate the present-day Greenland ice sheet using the GRISLI ice sheet model (version 1.3). Geoscientific Model Development, 2019, 12 (6), pp.2481-2499.10.5194/gmd-12-2481-2019 . hal-02328234

Machguth, H., H.H. Thomsen, W. Weidick, A.P. Ahlstrøm, J. Abermann, M. Andersen, S.B. Andersen, A.A. Bjørk, J.E. Box, R. Braithwaite, C.E. Bøggild, M. Citterio, P. Clement, W. Colgan, R.S. Fausto, K. Gleie, S. Gubler, B. Hasholt, B. Hynek, N.T. Knudsen, S.H. Larsen, S.H. Mernild, J. Oerlemans, H. Oerter, O.B. Olsen, C.J.P. Smeets, K. Steffen, M. Stober, S. Sugiyama, S. van As, M.R. van den Broeke and R.S.W. van de Wal.: Greenland surface mass-balance observations from the ice-sheet ablation area and local glaciers, Journal of Glaciology. 62: 861-887, doi: 10.1017/jog.2016.7, 2016.

Machguth, H.: Historical surface mass balance measurements from the ice-sheet ablation area and local glaciers, https://doi.org/10.22008/FK2/5VNBQA, GEUS Dataverse, V1, 2022. [Last access 16/07/2022].

Mark, D. M., and Aronson, P. B.: Scale-dependent fractal dimensions of topographic surfaces: an empirical investigation, with applications in geomorphology and computer mapping, Journal of the International Association for Mathematical Geology, 16, 671-683, 1984.

Noël, B., van de Berg, W. J., Machguth, H., Lhermitte, S., Howat, I., Fettweis, X., and Van Den Broeke, M. R.: A daily, 1 km resolution data set of downscaled Greenland ice sheet surface mass balance (1958–2015), The Cryosphere, 10(5), 2361-2377, 2016.

Noël B, van de Berg, W. J., Lhermitte, S., and van den Broeke, M. R.: Rapid ablation zone expansion amplifies north Greenland mass loss, Sci Adv., 5, eaaw0123, https://doi.org/10.1126/sciadv.aaw0123, 2019.

Noh, M. J., and Howat, I. M.: Automated stereo-photogrammetric DEM generation at high latitudes: Surface Extraction with TIN-based Search-space Minimization (SETSM) validation and demonstration over glaciated regions, GIScience & Remote Sensing, 52.2 (2015): 198-217, 2015.

Porter, C., Morin, P., Howat, I., Noh, M. J., Bates, B., Peterman, K., Keesey, S., Schlenk, M., Gardiner, J., Tomko, K., Willis, M., Kelleher, C., Cloutier, M., Husby, E., Foga, S., Nakamura, H., Platson, M., Wethington, M. Jr., Williamson, C., Bauer,

G., Enos, J., Arnold, G., Kramer, W., Becker, P., Doshi, A., D'Souza, C., Cummens, P., Laurier, F., Bojesen, M.: ArcticDEM, Harvard Dataverse, https://doi.org/10.7910/DVN/OHHUKH, 2018. [Last access 16/02/2023].

Smith, B. E., Medley, B., Fettweis, X., Sutterley, T., Alexander, P., Porter, D., & Tedesco, M. (2023). Evaluating Greenland surface-mass-balance and firn-densification data using ICESat-2 altimetry. The Cryosphere, 17(2), 789-808. https://doi.org/10.5194/tc-17-789-2023

Steffen, K., Houtz, D., Vandecrux, B., Abdalati, W., Bayou, N., Box, J., Colgan, W., Espona Pernas, L.; Griessinger, N., Haas-Artho, D., Heilig, A., Hubert, A., Iosifescu Enescu, I., Johnson-Amin, N., Karlsson, N. B., Kurup, R., McGrath, D., Naderpour, R., Pederson, A. Ø., Perren, B., Phillips, T., Plattner, G., Proksch, M., Revheim, M. K., Saettele, M., Schneebeli, M., Sampson, K., Starkweather, S., Steffen, S., Stroeve, J., Walter, B., Winton, Ø. A. and Zwally, J., Greenland Climate Network (GC-Net) Data., EnviDat 2020, https://www.doi.org/10.16904/envidat.1, 2020.

Tedesco, M., Fettweis, X., Mote, T., Wahr, J., Alexander, P., Box, J. E., and Wouters, B.: Evidence and analysis of 2012 Greenland records from spaceborne observations, a regional climate model and reanalysis data, The Cryosphere, 7, 615–630, https://doi.org/10.5194/tc-7-615-2013, 2013.

Tedesco, M., Cervone, G., Colosio, P. and Fettweis, X.: A computationally efficient statistically downscaled 100 m resolution Greenland product from the regional climate model MAR: accompanying dataset. https://doi.org/10.5281/zenodo.7803611

Vedyushkin, M. A.: Fractal properties of forest spatial structure, Vegetatio, 113, 65-70, 1994.

Wang, Z., Bovik, A. C., Sheikh, H. R. and Simoncelli, E. P., Image quality assessment: from error visibility to structural similarity, IEEE transactions on image processing, 13(4), 600-612, 2004.

Webster, R., and Oliver, M. A.: Geostatistics for environmental scientists, John Wiley & Sons, 2007.
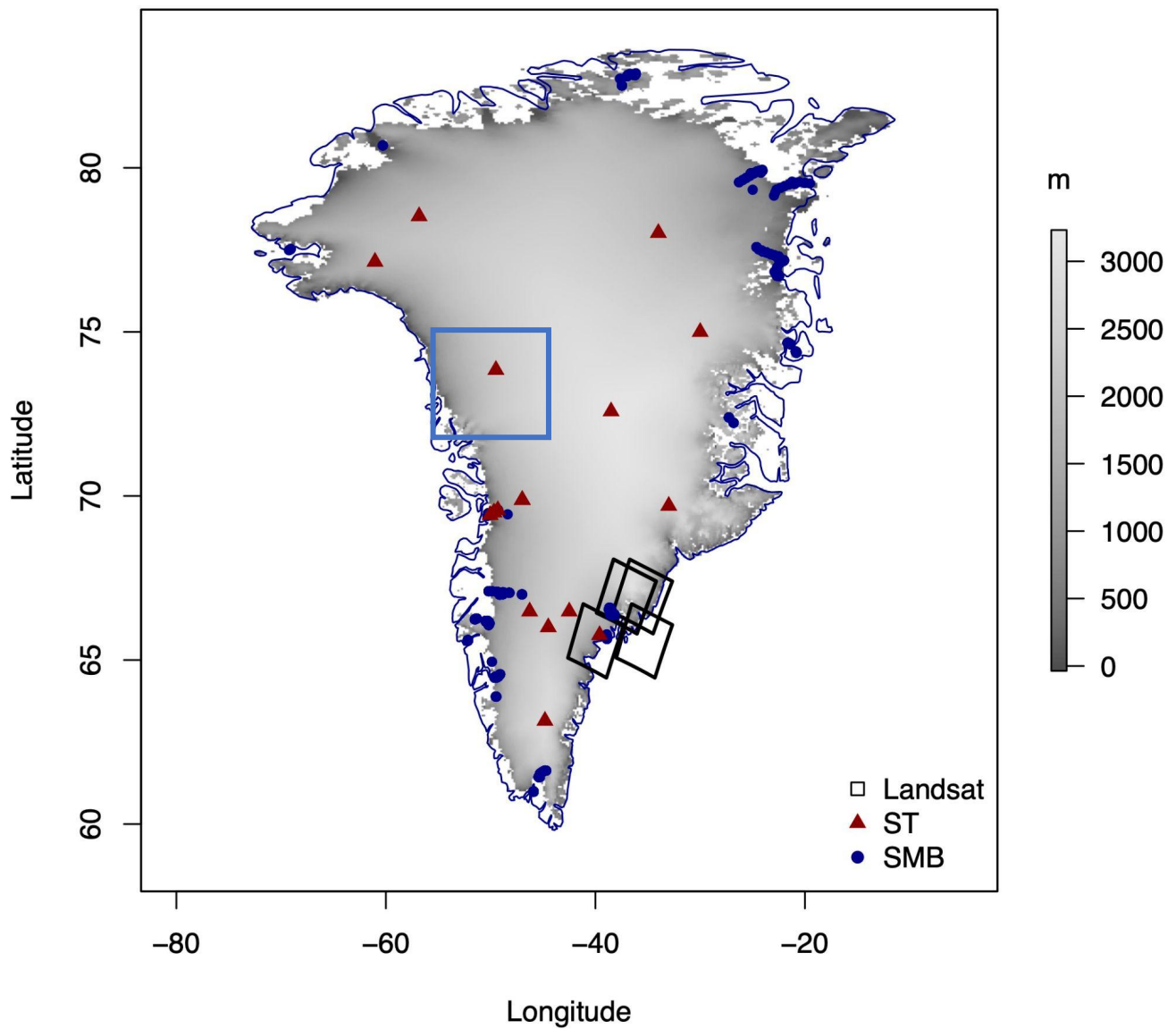
Figure 1: Map of Greenland ice sheet. The digital elevation model (DEM) at 100 m resolution is represented in greyscale, the GC-Net air temperature locations are plotted as red triangles and the PROMICE surface mass balance measurements locations are reported as blue dots. The two rectangles indicate the Jakobshavn (blue) and Helheim (black) regions.

ID	Glacier/Site name	Latitude [°]	Longitude [°]	Measurement years	Points	Readings
126	Qaanaaq Ice cap	77° 30' 36'' N	69° 9' 0'' W	2012-2015	6	12
128	Petermann	80° 41' 2'' N	60° 17' 35'' W	2002-2013	2	4
130	Hans Tausen Ice Cap	82° 29' 24''	37° 30' 0'' W	1995 and earlier	5	13
140	Hare Glacier	82° 50' 24'' N	36° 40' 12'' W	1994-95	29	62
170	Kronprins Christian Land	79° 46' 48'' N	25° 11' 24'' W	1993-1994, 2008-2013	20	62
180	Nioghalfvjerdsfjorden	79° 30' 0'' N	21° 36' 0'' W	1996-1997	13	13
215	Storstrømmen	77° 30' 0'' N	23° 0' 0'' W	1989-1994	22	113
220	A.P. Olsen Ice Cap	74° 38' 24'' N	21° 26' 60'' W	2008-2013	17	56
230	Freya Glacier	74° 22' 48'' N	20° 49' 12'' W	2008-2013	29	93
232	Violin Glacier	72° 20' 60'' N	26° 58' 48'' W	2008-2013	2	12
254	Helheim	66° 24' 36'' N	38° 20' 24'' W	2008-2010	21	118
270	Isertoq	65° 42' 0'' N	38° 53' 24'' W	2007-2013	2	15
315	Nordbo Glacier	61° 30' 0'' N	45° 22' 12'' W	1977-83	41	200
412	Isortuarssup Sermia	63° 47' 60'' N	49° 47' 60'' W	1983-1988	3	9
414	Qamanarssup Sermia	64° 30' 0'' N	49° 23' 60'' W	1979-1988, 2007-2013	20	164
416	Kangilinnguata Sermia	64° 52' 48'' N	49° 17' 60'' W	2010-2013	1	3
420	Qapiarfiup	65° 34' 48'' N	52° 12' 36'' W	1980-1989	5	75
440	Amitsuloq Ice Cap	66° 8' 24'' N	50° 19' 12'' W	1981-1990	26	422
450	Tasersiaq	66° 15' 36'' N	51° 23' 60'' W	1982-1989	6	111
454	K-Transect	67° 5' 60'' N	48° 51' 36'' W	1990-2013	11	193
456	Paakitsoq, JAR	69° 29' 24'' N	49°51' 36'' W	1982-1992, 1996-2013	22	220

| 458 | Swiss Camp/ST2 | 69° 33' 53'' N | 49° 19' 51'' W | 1990-2014 | 2 | 12 |

Table 1: PROMICE surface mass balance measurements information for the selected Glaciers and measurements sites.
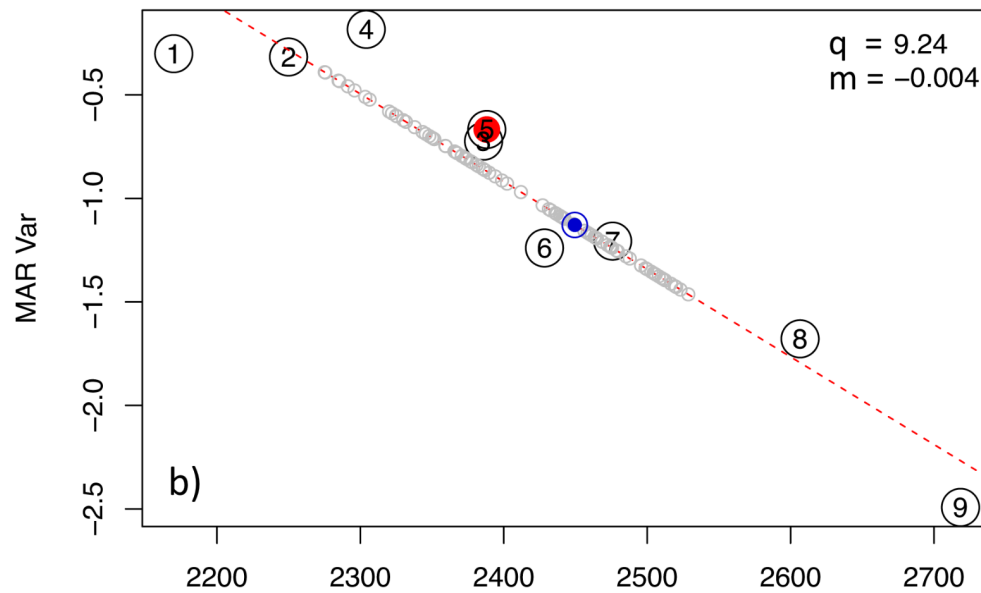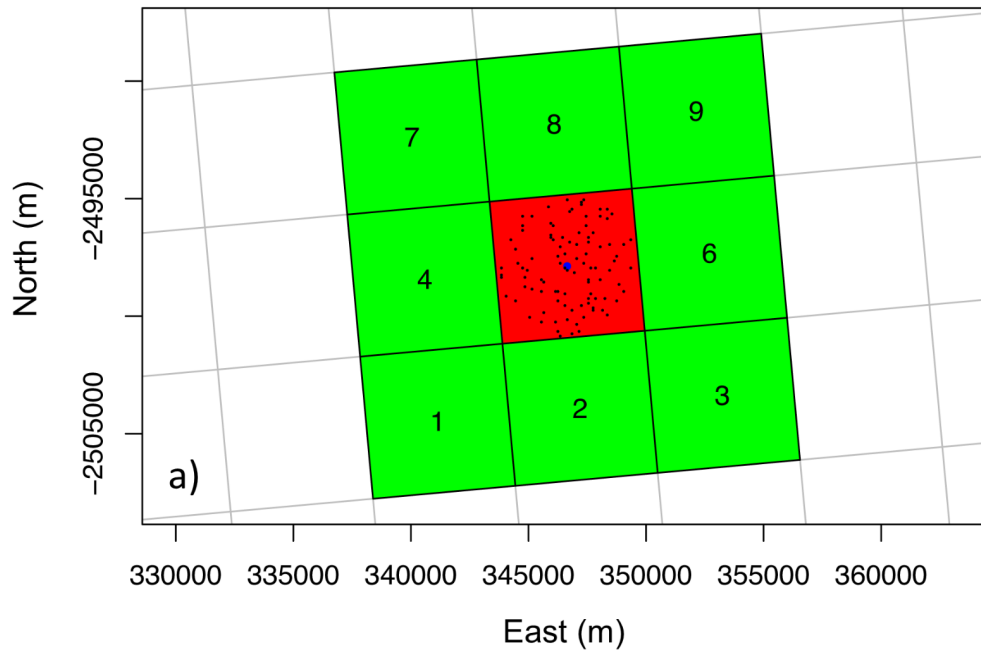
Figure 2: Elevation downscaling procedure example for a generic variable. In panel (a) the considered MAR pixel (red) and the surrounding pixels (green) adopted for the local linear regression are represented. The blue dot represents 100 m pixel location centered within the considered MAR pixel. In panel (b) the variable value of each considered pixel is reported as numbered circle. The dashed red line represents the linear regression computed for such pixels, the blue circle represents the downscaled variable for the blue pixel in panel (a) and the grey circles represent the downscaled variable for a group of 100 m pixels randomly picked within the considered MAR pixel which locations are represented as black dots in panel (a).

Station	Latitude [°]	Longitude [°]	Elevation [m]	R_2 MAR$_{6km}$	R_2 MAR$_{100m}$	RMSE MAR$_{6km}$	RMSE MAR$_{100m}$
Swiss Camp	69° 34' 06" N	49° 18' 57" W	1149	0.945	0.945	2.37	2.36
Crawford Pt.1	69° 52' 47" N	46° 59' 12" W	2022	0.872	0.873	3.95	3.95
NASA-U	73° 50' 31" N	49° 29' 54" W	2369	0.788	0.789	5.35	5.34
GITS	77° 08' 16" N,	61° 02' 28" W	1887	0.915	0.915	3.4	3.4
Humboldt	78° 31' 36" N	56° 49' 50" W	1995	0.801	0.801	5.64	5.64
Summit	72° 34' 47" N	38° 30' 16" W	3254	0.837	0.84	4.62	4.58
Tunu-N	78° 01' 0" N	33° 59' 38" W	2113	0.937	0.936	3.17	3.2
DYE2	66° 28' 48" N	46° 16' 44" W	2165	0.94	0.94	2.72	2.72
JAR1	69° 29' 54" N	49° 40' 54" W	962	0.787	0.786	4.37	4.38
Saddle	66° 00' 02" N	44° 30' 05" W	2559	0.935	0.935	2.77	2.77
South Dome	63° 08' 56" N	44° 49' 00" W	2922	0.915	0.915	2.76	2.77
NASA-E	75° 00' 00" N	29° 59' 59" W	2631	0.882	0.881	3.94	3.97
Crawford Pt.2	69° 54' 48" N	46° 51' 17" W	1990	0.893	0.894	3.62	3.61
NASA-SE	66° 28' 47" N	42°30' 00" W	2425	0.86	0.86	3.83	3.83
KAR	69° 41' 58" N	33° 00' 21" W	2579	0.935	0.936	2.6	2.57
JAR2	69º 25' 12" N	50º 03' 27" W	568	0.706	0.709	4.79	4.76
KULU	65° 45' 30" N	39° 36' 06" W	878	0.59	0.595	5.22	5.19

34
35 **Table 2: Root-mean-square error and R^2 computed comparing MAR$_{6km}$ and MAR$_{100m}$ with air temperature measurements from the**
36 **GC-Net considered stations. Longitude, latitude and elevation of the station are also reported.**

37

38
39

(a)

40
41

(b)

(c)
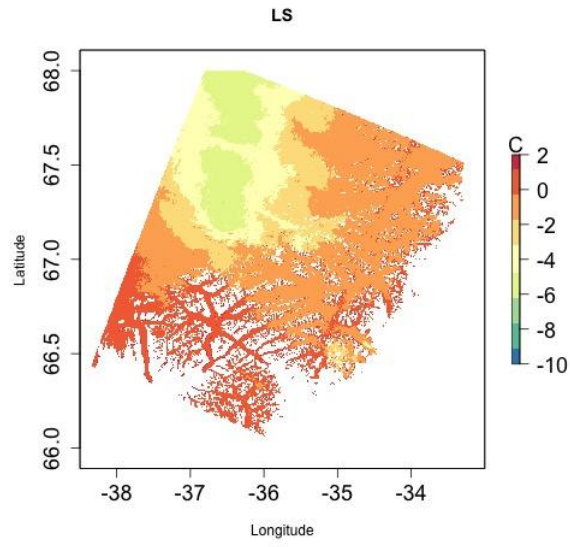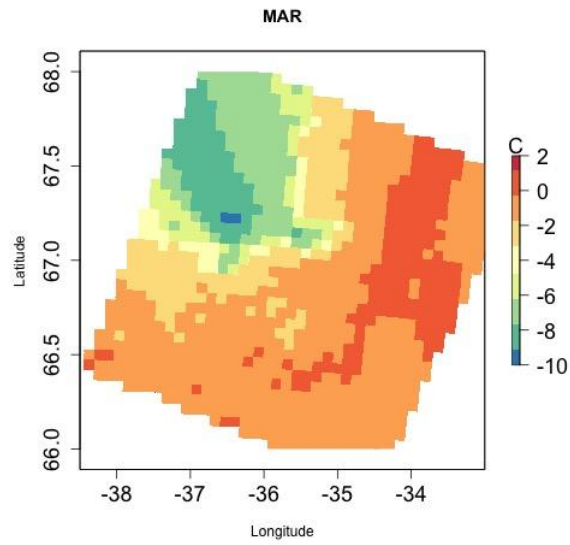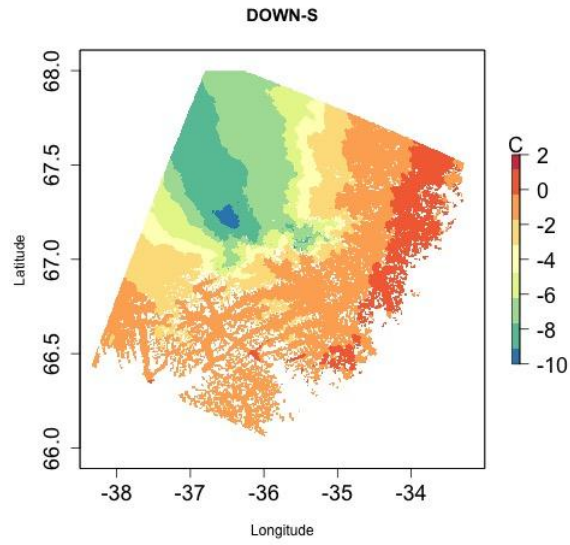
Figure 3: Maps of temperature from (a) Landsat-8, (b) MAR$_{6km}$v2 and (c) MAR$_{100m}$ over the area covered by the Landsat 8 selected image on 30 June 2015. The blue dot reported to every map represents the 6 km pixel of the original MAR grid reported in red in Figure 2a.
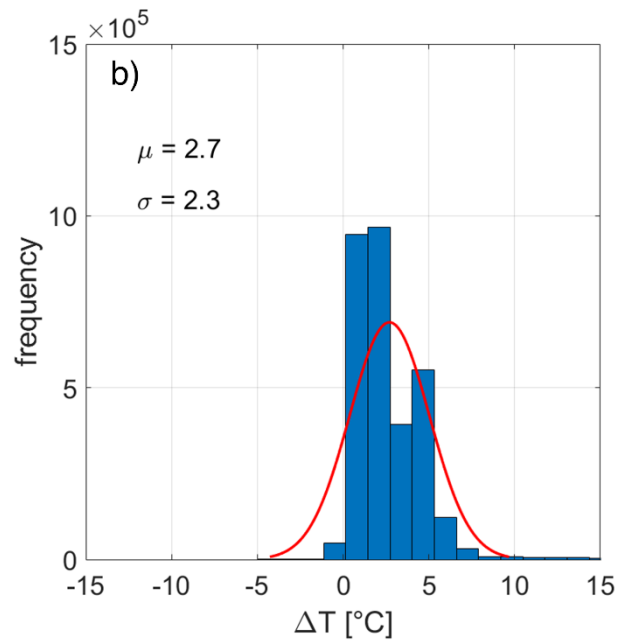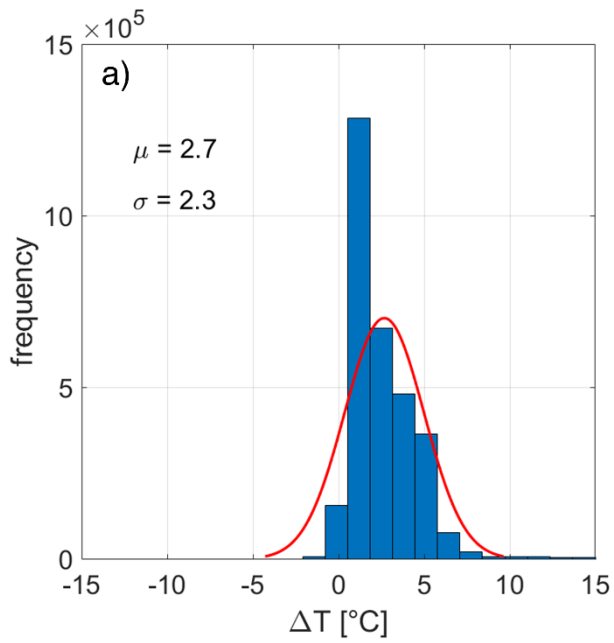
49
50 **Figure 4: Histograms of the difference (a) between the 6 km MAR temperature and Landsat-8 temperature and (b) between 100 m**
51 **MAR temperature and Landsat-8 temperature.**

52

53
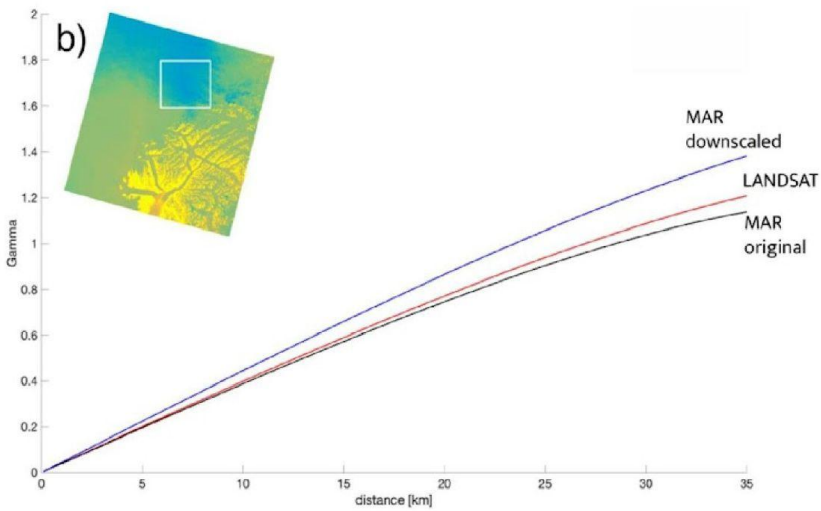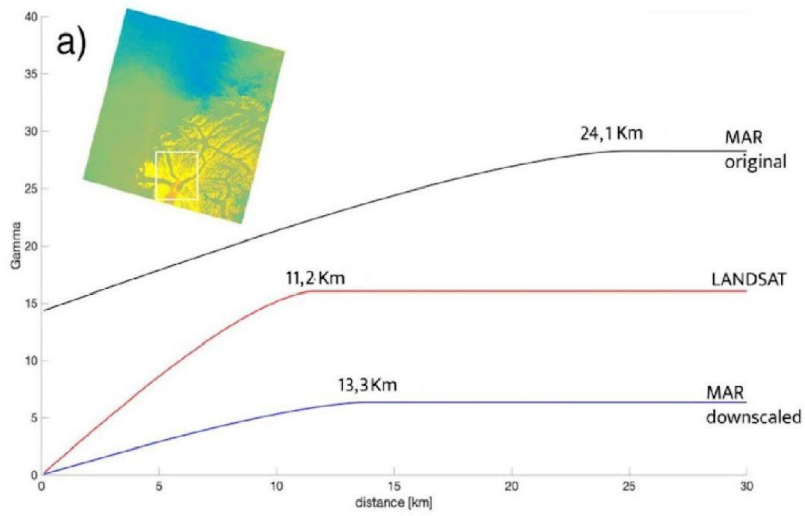
54
55
56 **Figure 5: Modeled   semi variograms for the Landsat-8, MAR$_{6km}$ and MAR$_{100m}$ computed over two regions of interest reported in**
57 **the inset.**

58
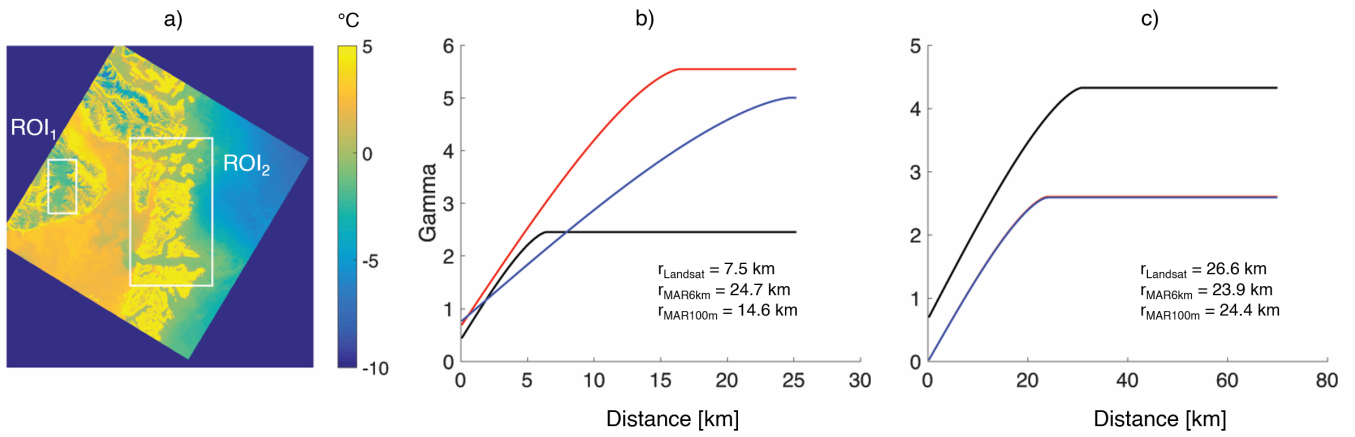
59
60 **Figure 6: (a) Landsat-8 temperature captured on 11 June 2015 over areas around the Jakobshavn Glacier and (b, c) modeled semi**
61 **variograms for the Landsat-8, MAR$_{6km}$ and MAR$_{100m}$ computed over (b) the first region of interest (ROI$_1$) and (b) the second region**
62 **of interest (ROI$_2$).**

63

a)

b)
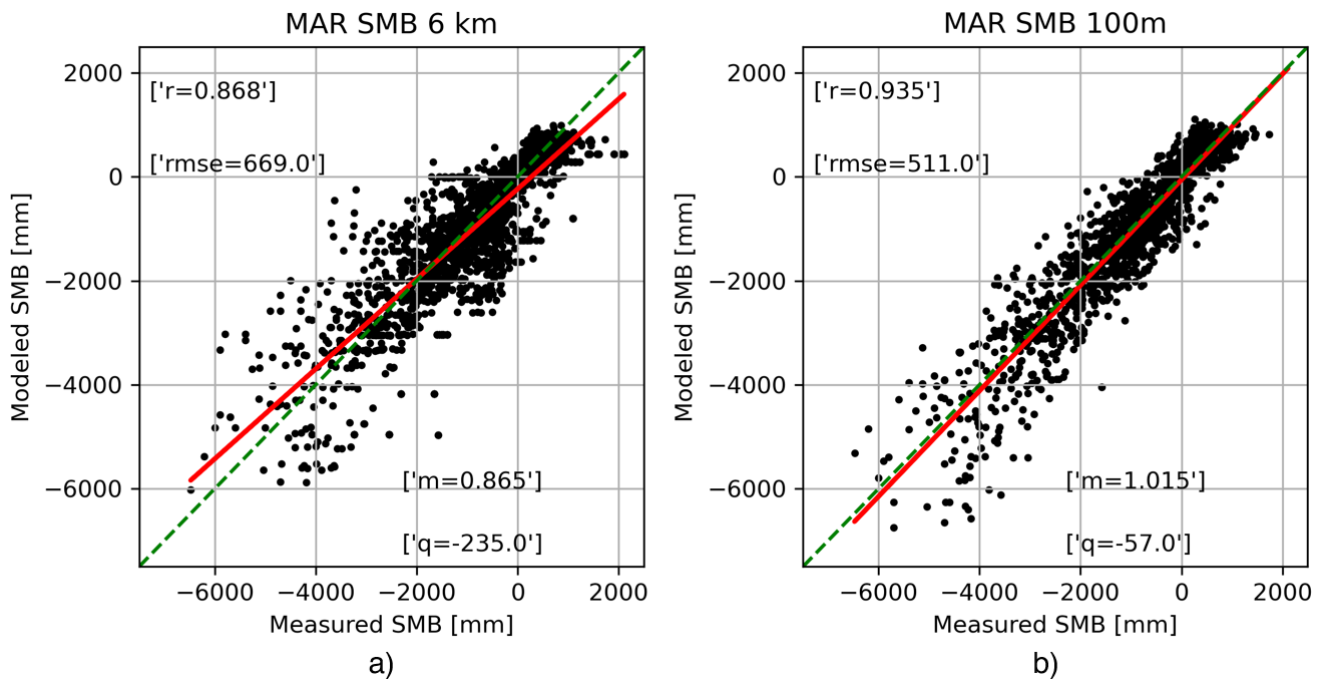
Figure 7: Comparison between measured and modeled surface mass balance from (a) original 6 km MAR and (b) downscaled
100 m MAR.
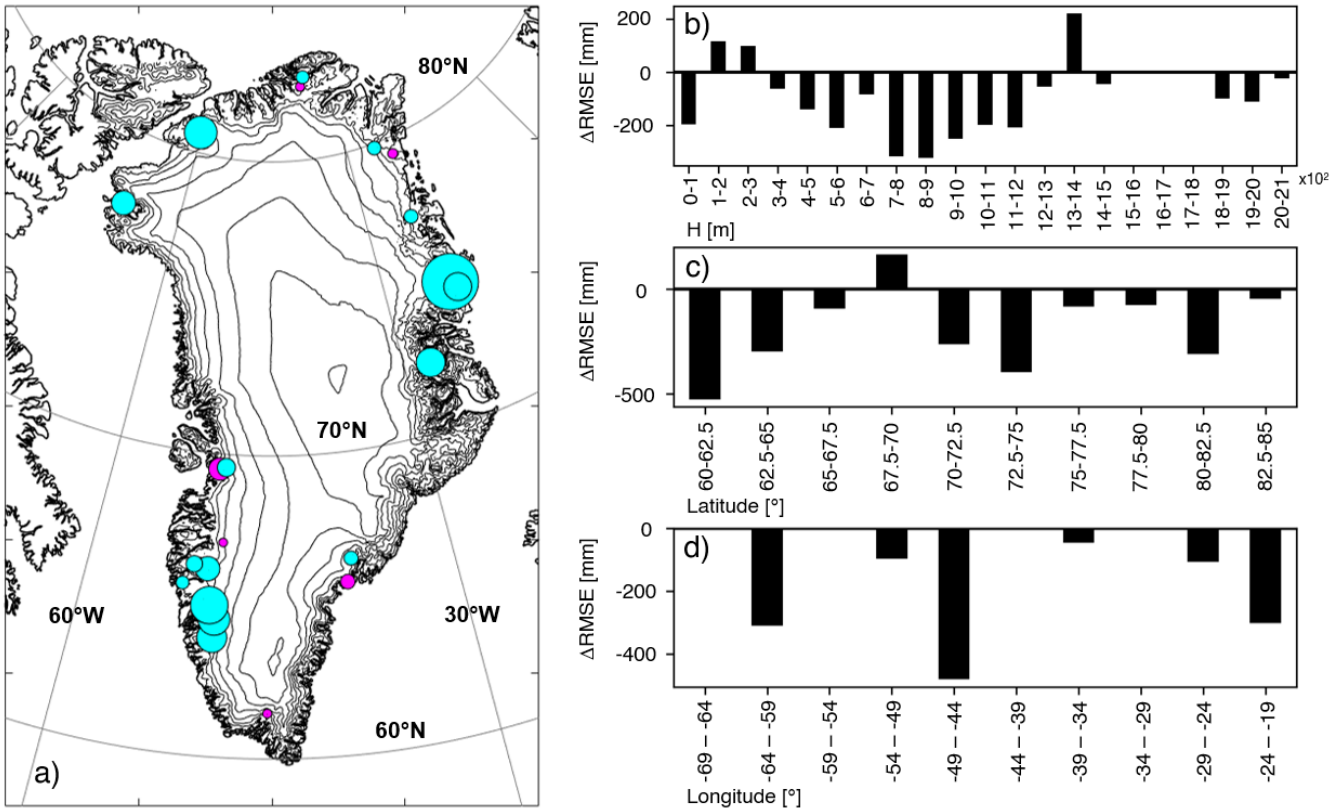
68
69 **Figure 8: Difference between original and downscaled MAR modeled   surface mass balance RMSE with respect to the measured**
70 **surface mass balance data (RMSE$_{100m}$-RMSE$_{6km}$) by (a) glacier, (b) elevation, (c) latitude and (d) longitude. In the bubble chart map**
71 **the contour lines are plotted every 500 m (original MAR$_{6\ km}$ DEM), positive values (worsening) of ΔRMSE are reported in magenta**
72 **while negative values (improvement) in cyan.**

73